Draft version August 14, 2020
Typeset using LaTeX default style in AASTeX63

Starspot mapping with adaptive parallel tempering I: Implementation of computational code

Kai Ikuta,[1] Hiroyuki Maehara,[2,3] Yuta Notsu,[4,5] Kosuke Namekata,[1] Taichi Kato,[1] Shota Notsu,[6,*] Soshi Okamoto,[1] Satoshi Honda,[7] Daisaku Nogami,[1] and Kazunari Shibata[3]

[1]*Department of Astronomy, Kyoto University, Kitashirakawa-Oiwake-cho, Sakyo, Kyoto, Kyoto 606-8502, Japan*
[2]*Okayama Branch Office, Subaru Telescope, National Astronomical Observatory of Japan, NINS, Kamogata, Asakuchi, Okayama 719-0232, Japan*
[3]*Astronomical Observatory, Kyoto University, Kitashirakawa-Oiwake-cho, Sakyo, Kyoto 606-8502, Japan*
[4]*Laboratory for Atmospheric and Space Physics, University of Colorado Boulder, 3665 Discovery Drive, Boulder, Colorado 80303, USA*
[5]*National Solar Observatory, 3665 Discovery Drive, Boulder, Colorado 80303, USA*
[6]*Leiden Observatory, Faculty of Science, Leiden University, PO Box 9513, 2300 RA Leiden, The Netherlands*
[7]*Nishi-Harima Astronomical Observatory, University of Hyogo, 407-2, Nishigaichi, Sayo-cho, Sayo, Hyogo 679-5313, Japan*

(Received April 30, 2020; Revised July 21, 2020; Accepted August 10, 2020)

Submitted to ApJ

ABSTRACT

Starspots are thought to be regions of locally strong magnetic fields, similar to sunspots, and they can generate photometric brightness modulations. To deduce stellar and spot properties, such as spot emergence and decay rates, we implement computational code for starspot modeling. It is implemented with an adaptive parallel tempering algorithm and an importance sampling algorithm for parameter estimation and model selection in the Bayesian framework. For evaluating the performance of the code, we apply it to synthetic light curves produced with 3 spots. The light curves are specified in the spot parameters, such as the radii, intensities, latitudes, longitudes, and emergence/decay durations. The spots are circular with specified radii and intensities relative to the photosphere, and the stellar differential rotation coefficient is also included in the light curves. As a result, stellar and spot parameters are uniquely deduced. The number of spots is correctly determined: the 3-spot model is preferable because the model evidence is much greater than that of 2-spot models by orders of magnitude and more than that of 4-spot model by a more modest factor, whereas the light curves are produced to have 2 or 1 local minimum during one equatorial rotation period by adjusting the values of longitude. The spot emergence and decay rates can be estimated with error less than an order of magnitude, considering the difference of the number of spots.

Keywords: Starspots, Bayesian statistics, Markov chain Monte Carlo, Importance sampling, Model selection, Astrostatistics

1. INTRODUCTION

Corresponding author: Kai Ikuta
ikuta@kusastro.kyoto-u.ac.jp

* Current Affiliation: Star and Planet Formation Laboratory, RIKEN Cluster for Pioneering Research, 2-1 Hirosawa, Wako, Saitama 351-0198, Japan

Starspots are apparent manifestations of magnetic activity on the stellar surface, and can be ubiquitously observed on various types of stars (for reviews, see Berdyugina 2005; Strassmeier 2009). For active young stars, cool stars, and RS CVn-type stars, starspots have been extensively studied through ground-based observations (e.g., Henry et al. 1995). With the advent of unprecedented precision and long-term photometry by the *Kepler* space telescope (Koch et al. 2010), photometric brightness modulations ascribed to spots have facilitated studies of starspot properties (e.g., Basri et al. 2010). There are some components to elucidate stellar magnetic activities analogous to solar ones. The most remarkable ones are the distribution of spot latitude (Morris et al. 2017) and the degree of differential rotation (Reinhold et al. 2013). It is also significant to measure the emergence and decay rates of starspots (e.g., Toriumi & Wang 2019; Namekata et al. 2019) because they relate to the following issues: (i) Solar flares tend to be driven by emerging sunspots (Toriumi & Wang 2019), and superflares could occur on solar-type stars (Maehara et al. 2012; Shibayama et al. 2013; Karoff et al. 2016; Maehara et al. 2017; Notsu et al. 2019) because large spots can cause them (Shibata et al. 2013). (ii) Measuring magnetic diffusion of the convection zone must be constrained for theoretical stellar dynamo (e.g., Bradshaw & Hartigan 2014). To measure the temporal evolution of starspots on solar-type stars, light curve analyses of spotted stars have been employed by utilizing the rotational brightness modulations (Namekata et al. 2019) and transiting exoplanet occultations (Davenport 2015; Namekata et al. 2020). Furthermore, light curve inversion or starspot mapping (hereinafter, referred to as starspot modeling) has also been performed to decipher starspot properties on the stellar surface (e.g., Strassmeier & Bopp 1992; Savanov & Strassmeier 2008; Mosser et al. 2009), especially on the basis of Bayesian inference (Croll 2006; Croll et al. 2006; Walker et al. 2007; Frasca et al. 2011; Lanza et al. 2014; Almenara et al. 2018) using the Markov chain Monte Carlo algorithm (MCMC; Foreman-Mackey et al. 2013; Sharma 2017; Hogg & Foreman-Mackey 2018). Walker et al. (2007) also implemented a parallel tempering algorithm (PT; Hukushima & Nemoto 1996; Gregory 2005a,b; Vousden et al. 2016; Sharma 2017) in `StarSpotz` code (Croll 2006; Croll et al. 2006) to explore multi-dimensional parameter space more efficiently.

For the purpose of deducing stellar and spot properties from the photometric brightness modulations, we implement computational code for starspot modeling. It is implemented with an adaptive parallel tempering algorithm and an importance sampling algorithm for parameter estimation and model selection in the Bayesian framework (cf. Neal 1996, 2001). The adaptive parallel tempering algorithm is based on the PT algorithm together with an adaptive algorithm (Haario et al. 2001; Andrieu & Thoms 2008; Araki & Ikeda 2013). Compared with `StarSpotz` code (Walker et al. 2007), we adopt the more sophisticated spotted model, including spot emergence and decay durations (Kipping 2012). Furthermore, the number of spots on the stellar surface can play an important role in measuring the emergence and decay rates. Several studies have investigated how the number of spots is related to light curves (e.g., Eker 1994; Notsu et al. 2013b; Morris et al. 2017; Basri & Nguyen 2018; Basri 2018; Namekata et al. 2020). We determine the number of spots based on model selection, computing the value of each model evidence by the importance sampling algorithm (e.g., Kass & Raftery 1995; Díaz et al. 2014).

In this study, to evaluate the performance of the code, we revisit synthetic light curves emulating *Kepler* data of spotted stars. We qualitatively evaluate how the above-described stellar and spot properties can be deduced from the photometric brightness modulations under appropriate assumptions toward conducting starspot modeling for photometric data obtained by *Kepler* and *Transiting Exoplanet Survey Satellite* (*TESS*) (Paper II; Ikuta et al. 2020 in preparation). The remainder of this paper is organized as follows. In Section 2, we describe the algorithms based on Bayesian inference and a numerical setup for starspot modeling. In Section 3, we discuss the results of starspot

modeling in terms of parameter degeneracies, determining the number of spots, and their effects on the spot emergence and decay rates. In Section 4, we conclude this paper and describe future prospects to deal with real data.

2. METHOD

2.1. *Bayesian inference: Adaptive parallel tempering algorithm*

According to Bayes' theorem, the posterior distribution equals a product of the likelihood and the prior distribution normalized by the model evidence $\mathcal{Z}$:

$$p(\theta|\mathcal{D}, M) = \frac{p(\mathcal{D}|\theta, M)p(\theta|M)}{\mathcal{Z}}, \quad \mathcal{Z} = p(\mathcal{D}|M) = \int p(\mathcal{D}|\theta, M)p(\theta|M)d\theta, \tag{1}$$

where θ, $\mathcal{D}$, and M denote modeled parameters, observed data, and the assumed model, respectively. In Bayesian inference, we compute the posterior distribution of the modeled parameters θ. However, in multi-dimensional cases of more than several parameters, it becomes extremely difficult to compute the denominator of Equation (1) as the normalization constant of the posterior distribution. In such cases, we usually use the Monte Carlo method as an approximation of inference sampling. In particular, for deducing the posterior distribution of such multi-dimensional parameters, the Markov chain Monte Carlo (MCMC) algorithm has extensively been used in astronomical context (Ford 2005, 2006; Foreman-Mackey et al. 2013; Nelson et al. 2014; Sharma 2017; Hogg & Foreman-Mackey 2018). Especially in the case of starspot modeling of photometric data, the MCMC algorithm has been applied to photometic data obtained by *Microvariability and Oscillations of Stars* (*MOST*) (`StarSpotz`; Croll 2006; Croll et al. 2006; Walker et al. 2007) and *Kepler* data (Frasca et al. 2011; Fröhlich et al. 2012; Lanza et al. 2014; Almenara et al. 2018). The MCMC algorithm can generate samples that follow the posterior distribution with a proposal distribution. However, in the case of a multi-modal and multi-dimensional posterior distribution, the produced MCMC samples can be trapped in local maxima for so many iterations. Thus, the parallel tempering (PT) algorithm is occasionally implemented to circumvent this problem as in `StarSpotz` code (Walker et al. 2007). The PT algorithm introduces auxiliary distributions with a tempering parameter β_l : $\pi_l(\theta) \equiv \{p(\mathcal{D}|\theta)\}^{\beta_l} p(\theta)$ $(1 = \beta_1 > \cdots > \beta_l > \cdots > 0)$, where $\pi_1(\theta)$ corresponds to the posterior distribution $p(\theta|\mathcal{D})$ except the normalization constant. Hereby, β_l tempers the multi-modality of the likelihood $p(\mathcal{D}|\theta)$, and the peaks become less pronounced as $\beta_l \to 0$. It becomes easier for the corresponding Markov chain to step away from a local maximum, and chains with smaller β_l are more readily able to explore the full parameter space.

The PT algorithm generates multiple MCMC samples from the posterior distribution and the auxiliary distributions in parallel, and exchanges the samples of two chains between a pair of adjacent chains only for some steps. This tempering implementation and the exchange process enable local maxima to be circumvented. The PT algorithm executes either transition or exchange at every iteration step with a probability α_r or $1 - \alpha_r$, respectively. The value of α_r is determined by exploiting the trial runs, and we set $\alpha_r = 0.10$. At transition steps, as specified in the MCMC algorithm, for each l a proposed θ_l for the next iteration is drawn from a proposal distribution that is chosen to be a normal distribution characterized by a variance-covariance matrix Σ_l. The proposed θ_l is accepted or rejected according to the Metropolis-Hastings algorithm (Metropolis et al. 1953; Hastings 1970). At the exchange step, a sample θ_l is randomly selected and exchanged for θ_{l+1} with probability of $\min\{(1, \pi_l(\theta_{l+1})\pi_{l+1}(\theta_l)/\pi_l(\theta_l)\pi_{l+1}(\theta_{l+1})\}$.

The performance of the PT algorithm strongly depends on the tempering parameters specifically determined by their intervals, number, and proposal parameters Σ_l. These must be selected so that each chain converges as fast as possible. They should be finely tuned by trial-and-error in test computations so far because their relation to the number of iterations until convergence has been unclear. Then, the adaptive algorithm for the Metropolis-Hastings algorithm is

investigated in the statistical framework (Haario et al. 2001; Andrieu & Thoms 2008) and applied to astronomical data (Yamada et al. 2020) so that the MCMC acceptance rate in multi-dimensional case approximately converges to the optimal value = 0.25 (Roberts et al. 1997). Furthermore, Araki & Ikeda (2013) investigates the adaptive algorithm for the PT algorithm so that the PT exchange rate between adjacent chains approximately converges to the optimal value = 0.25 (Roberts et al. 1998).

The adaptive algorithm adjusts the proposal parameters using past samples during iterations on the basis of the Robbins-Monro algorithm (Robbins & Monro 1951). For adaptive Metropolis algorithm with adaptive scaling, normal proposal distribution $N(\theta_l, \sigma_l^2 \mathbf{\Sigma}_l)$ is employed as a scale factor σ_l^2 is factored out from $\mathbf{\Sigma}_l$, and $\mathbf{\Sigma}_l$ are rescaled (Andrieu & Thoms 2008). At the n-th transition step, the l-th proposal parameters are updated as

$$\mu_{l,n+1} \leftarrow \mu_{l,n} + a_n(\theta_{l,n} - \mu_{l,n}) \tag{2}$$

$$\mathbf{\Sigma}_{l,n+1} \leftarrow \mathbf{\Sigma}_{l,n} + a_n\big((\theta_{l,n} - \mu_{l,n})(\theta_{l,n} - \mu_{l,n})^{\mathrm{T}} - \mathbf{\Sigma}_{l,n}\big) \tag{3}$$

$$\sigma^2{}_{l,n+1} \leftarrow \sigma^2{}_{l,n} + a_n(FA_n - \alpha_{\mathrm{ac}}), \tag{4}$$

where μ_l is an auxiliary proposal parameter (expectation value of θ_l), and also updated $\mu_{l,n+1} \leftarrow \theta_{l,n+1}$ when $\theta_{l,n}$ is updated to $\theta_{l,n+1}$ by being exchanged for $\theta_{l-1,n}$ or $\theta_{l+1,n}$ at the exchange step. FA_n is one if the proposed sample is accepted or zero if it is rejected. $\alpha_{\mathrm{ac}} = 0.25$ is the optimal acceptance rate, which the MCMC acceptance rate should approaches with the proceeding of iteration (Roberts et al. 1997). At the n-th exchange step, l-th tempering parameter is updated as

$$\log \beta_{l,n+1} \leftarrow \log \beta_{l,n} - b_n(ER_{l,n} - \alpha_{\mathrm{ex}}). \tag{5}$$

$ER_{l,n}$ is one if parameters are exchanged or zero if not. $\alpha_{\mathrm{ex}} = 0.25$ is the optimal exchange rate, which the PT exchange rate approaches with the proceeding of iteration (Roberts et al. 1998). The learning coefficients a_n and b_n converge to zero when the number of iterations n approaches infinity. The details about the choice of the learning coefficients are described in Andrieu & Thoms (2008). In this study, we determined the number of iterations $N = 4 \times 10^6$ after the burn-in period $= 1 \times 10^6$ on the basis of the Gelman-Rubin convergence diagnostic (Gelman & Rubin 1992; Brooks & Gelman 1998). We set the learning coefficients $a_n = 1/(10n + N)$ and $b_n = 1/(n + N)$ so that the acceptance and exchange rates adequately converge to the moderate values, and the adaptive algorithms are executed after the burn-in period of the MCMC. In addition, we selected the number of parallelization $l = 10$ and the tempering parameters $\beta_l = \exp\{7(l-1)/2\}$ by exploiting the trial runs so that chains with small β_l are much easily able to transition in the full parameter space (cf., Vousden et al. 2016).

2.2. *Importance sampling algorithm*

For the purpose of model selection as determining the number of parameters, we compute model evidence (the denominator of Equation 1) using importance sampling algorithm along with parallel tempering transition. In Section 3.2, we compare the number of spots by the model evidence for 3-spots model, 2-spots models, and 4-spot model. We briefly introduce the importance sampling algorithm (Kass & Raftery 1995).

Model evidence is approximated by Monte Carlo integration with N samples as

$$\mathcal{Z} = \int p(\mathcal{D}|\theta, M)p(\theta|M)d\theta \simeq \frac{1}{N}\Sigma_{n=1}^{N} p(\mathcal{D}|\theta_n, M), \tag{6}$$

$$\text{where } \theta_n \text{ is drawn from } p(\theta|M). \tag{7}$$

However, computation of the summation becomes quite inefficient if most of the likelihood $p(\mathcal{D}|\theta, M)$ have small values and the posterior distribution $p(\theta|\mathcal{D}, M)$ concentrates on a small region of the parameter space. $\mathcal{Z}$ is dominated by a few large values of the likelihood.

To improve the precision of the Monte Carlo integration, the above formulation is deformed with importance sampling function $q(\theta|M)$ as

$$\mathcal{Z} = \int p(\mathcal{D}|\theta, M)\frac{p(\theta|M)}{q(\theta|M)}q(\theta|M)d\theta \simeq \frac{\Sigma_{n=1}^{N} w_n p(\mathcal{D}|\theta_n, M)}{\Sigma_{n=1}^{N} w_n}, \tag{8}$$

$$\text{where } w_n = \frac{p(\theta_n|M)}{q(\theta_n|M)} \text{ and } \theta_n \text{ is drawn from } q(\theta|M). \tag{9}$$

Adopting the posterior distribution $p(\theta|\mathcal{D}, M)$ as $q(\theta|M)$ since the samples can be drawn from the posterior distribution along with the PT transition, the model evidence $\mathcal{Z}$ is approximated as

$$\mathcal{Z} \simeq \left\{ \frac{1}{N}\Sigma_{n=1}^{N} p(\mathcal{D}|\theta_n, M)^{-1} \right\}^{-1}. \tag{10}$$

This value converges to the precise value of the model evidence $p(\mathcal{D}|M)$ when the number of samples N approaches infinity. Practically, we compute this value along with parallel tempering transition and use it for the model selection.

2.3. *Analytical spotted model*

According to Kipping (2012), a spotted flux at time t is described by the functions A and $\zeta_{\pm}$ of two parameters: the angular radius of the circular spot on the surface of the star as seen from the center of the star α and the angle between the line of sight and the line from the center of the star to the spot center β. The description summed up for the number of spots $N_{\rm spot}$ is formulated as

$$F(\boldsymbol{\alpha}, \boldsymbol{\beta}) = 1 - \sum_{j=0}^{4}\left(\frac{jc_j}{j+4}\right) - \sum_{k=1}^{N_{\rm spot}} \frac{A_k}{\pi}\left[\left(\sum_{j=0}^{4}\frac{4(c_j - d_j f_{\rm spot})}{j+4}\frac{\zeta_{+,k}^{(j+4)/2} - \zeta_{-,k}^{(j+4)/2}}{\zeta_{+,k}^2 - \zeta_{-,k}^2}\right)\right], \tag{11}$$

where

$$A_k = \begin{cases} \pi \sin^2\alpha_k \cos\beta_k & (0 < \beta_k < \pi/2 - \alpha_k) \\ \cos^{-1}[\cos\alpha_k \csc\beta_k] + \cos\beta_k \sin^2\alpha_k \cos^{-1}[-\cot\alpha_k \cot\beta_k] & \\ \qquad - \cos\alpha_k \sin\beta_k \sqrt{1 - \cos^2\alpha_k \csc^2\beta_k} & (\pi/2 - \alpha_k < \beta_k < \pi/2 + \alpha_k) \\ 0 & (\pi/2 + \alpha_k < \beta_k < \pi) \end{cases}$$

$$\zeta_{+,k} = \begin{cases} \cos(\beta_k + \alpha_k) & (0 < \beta_k < \pi/2 - \alpha_k) \\ 0 & (\pi/2 - \alpha_k < \beta_k < \pi) \end{cases}$$

$$\zeta_{-,k} = \begin{cases} 1 & (0 < \beta_k < \alpha_k) \\ \cos(\beta_k - \alpha_k) & (\alpha_k < \beta_k < \pi/2 + \alpha_k) \\ 0 & (\pi/2 + \alpha_k < \beta_k < \pi). \end{cases}$$

A_k is the sky-projected area visible to the observer of spot k, and the inequalities within parentheses involving α_k and β_k specify the conditions under which a spot is either fully visible on the near side of the star, partly visible, or fully invisible on the far side of the star, respectively. c_j, d_j $(j = 0, 1, 2, 3, 4)$, and $f_{\rm spot}$ are the stellar limb-darkening

coefficients, spot ones, and spot intensity relative to the photosphere, respectively. The temporal variation of α_k is represented by a trapezoidal function with time t (Figure 1 in Kipping 2012). Then, α_k and β_k relate to each spot and stellar parameter as

$$\alpha_k = \begin{cases} \alpha_{\max,k}\{t-(t_k-\mathcal{L}_k/2-\mathcal{I}_k)\}/\mathcal{I}_k & (t_k-\mathcal{L}_k/2-\mathcal{I}_k<t<t_k-\mathcal{L}_k/2) \\ \alpha_{\max,k} & (t_k-\mathcal{L}_k/2<t<t_k+\mathcal{L}_k/2) \\ \alpha_{\max,k}\{(t_k+\mathcal{L}_k/2+\mathcal{E}_k)-t\}/\mathcal{E}_k & (t_k+\mathcal{L}_k/2<t<t_k+\mathcal{L}_k/2+\mathcal{E}_k) \\ 0 & (t<t_k-\mathcal{L}_k/2-\mathcal{I}_k, t_k+\mathcal{L}_k/2+\mathcal{E}_k<t) \end{cases}$$

$$\cos\beta_k = \cos i \sin\Phi_k + \sin i \cos\Phi_k \cos\{\Lambda_k + \frac{2\pi}{P(\Phi_k)}t\} \tag{12}$$

$$\text{where} \quad P(\Phi_k) = \frac{P_{\rm eq}}{1-\kappa\sin^2\Phi_k}, \tag{13}$$

where $\alpha_{\max,k}$, t_k, $\mathcal{I}_k$, $\mathcal{E}_k$, and $\mathcal{L}_k$ are maximum radius, reference time (the time at the midpoint of the interval over which the spot has its maximum radius), emergence duration, decay duration, and stable duration, respectively. Each spot latitude Φ_k is assumed to be invariable, and each longitude is assumed to vary with time from the initial longitude Λ_k. The rotation period at the latitude Φ_k is characterized by equatorial period $P_{\rm eq}$ and the degree of differential rotation κ as solar-like differential rotation. The limb-darkening law is adopted as a quadratic term:

$$I(\mu)/I(1) = 1-u_1(1-\mu)-u_2(1-\mu)^2, \tag{14}$$

where μ represents the cosine of the azimuthal angle. Then, the limb-darkening coefficients are set as $c_1 = c_3 = d_1 = d_3 = 0, c_2 = d_2 = u_1+2u_2, c_4 = d_4 = -u_2$, and $c_0 = d_0 = 1-u_1-u_2$. We adopt solar values of the limb-darkening coefficients $c_2 = d_2 = 0.93, c_4 = d_4 = -0.23$ (Cox 2000). When applied to *Kepler* data of a spotted star, the limb-darkening coefficients can be adopted, dependent on the stellar parameters (Sing 2010).

2.4. *Numerical Setup*

We employ a normal likelihood function as

$$p(\mathcal{D}|\theta) = \prod_i \frac{1}{\sqrt{2\pi\sigma_i^2}} \exp\left[-\frac{\left(F_{{\rm obs},i}-F_{{\rm mod},i}(\theta)\right)^2}{2\sigma_i^2}\right] \tag{15}$$

$$\text{and} \quad F_{{\rm mod},i}(\theta) = F(\boldsymbol{\alpha}_i, \boldsymbol{\beta}_i)/F_{\rm ave} - 1, \tag{16}$$

where σ_i, $F_{{\rm obs},i}$, $F_{{\rm mod},i}(\theta)$, and $F_{\rm ave}$ are photometric error, relative flux scaled as Equation 16 for synthetic data emulated as observation, relative model flux characterized by parameters θ at the time t_i, and the average of $F(\boldsymbol{\alpha}_i, \boldsymbol{\beta}_i)$, respectively.

In Table 1 and 2, deduced parameters θ are denoted as the stellar and spot parameters: sine of inclination angle $\sin i$; equatorial rotation period $P_{\rm eq}$ (day); degree of differential rotation κ; relative intensity $f_{\rm spot}$; latitude Λ_k (deg); longitude Φ_k (deg); reference time t_k (day); maximum radius $\alpha_{\max,k}$ (deg); emergence duration $\mathcal{I}_k$ (day); decay duration $\mathcal{E}_k$ (day); and stable duration $\mathcal{L}_k$ (day). As each prior distribution, we selected truncated uniform, log-uniform (Jeffery's prior), and normal distributions; it is shown that there are degeneracies between the inclination angle i and each spot latitude Φ, and between the spot intensity $f_{\rm spot}$ and each spot size α (Eker 1996; Walkowicz et al. 2013). Each spot is discerned by the range of the reference time t_k so that the spots are not replaced one

by one during the parallel tempering parameter transition as denoted in Table 1 and 2. Furthermore, in the case of $\sin i \sim 1$, there are degeneracies between each spot latitude Φ and each spot size α (cf. Figure 1 Namekata et al. 2020). In other words, similar light curves can be generated by either a large spot at high latitude or a small spot at low latitude. Whether each spot exists on northern or southern hemisphere is also indiscernible. Therefore, we constrain the inclination angle and spot intensity as truncated normal distributions under the currently achieved precision (Maehara et al. 2017; Notsu et al. 2019).

2.5. *Synthetic light curves toward Kepler data*

Hereafter, for the purpose of modeling *Kepler* data of spotted stars, we produced two synthetic light curves with 3 spots for approximately two *Kepler* quarters ($\sim$ 200 days) so that they have quasi-periodic modulations ascribed to the spots. These light curves are generated with the spotted model (Kipping 2012) in addition to random error ($\sim$ 10% of modulation amplitude), emulating most faint *Kepler* stars and assuming spot-dominated stars (Montet et al. 2017). The input values to produce the light curves are listed in Tables 1 and 2. Assuming inclination angle of a star is randomly distributed in real data, the expectation value equals 1 (rad) (Gray 2008). Then, the values of the inclination angle are set 60 (deg), and each value of the spot latitudes are determined to be less than the value of the inclination angle so that the spots can be visible and invisible by the stellar rotation. We note that it is difficult to deduce the parameters of always visible spots at higher latitudes than the inclination angle. Each value of the spot longitudes is determined so that the light curves have 2 or 1 local minimum during one equatorial rotation period by adjusting the values of longitude. Hereinafter, we call each of the light curves 2-spot-like or 1-spot-like, respectively. In 45-deg and 30-deg cases of the inclination angle, we also produced such light curves and optimized them as well as the 60-deg case. Thereby, we ascertained the accuracies of the deduced parameters are almost the same as that of the 60-deg case by exploiting the test runs. This is because the accuracy of the posterior distribution of the inclination angle depends on its variance of the prior distribution, and this reflects the deduced accuracies of other parameters with degeneracies with the inclination angle. Although stellar continuum level is unknown due to some effects such as polar spots (e.g., Basri 2018), it is assumed to be invariant for the interval of the light curves because large spots are suggested to live for a few hundred days (Giles et al. 2017).

3. RESULTS AND DISCUSSION

We optimize 2-spot-like and 1-spot-like light curves by 3-spot model, 2-spot model, and 2-spot model with fixed inclination angle $\sin i$. In each case, unimodal posterior distributions are deduced. In the 3-spot model, the modes approximately equal the input values producing the light curves. In the 2-spot model, deduced posterior distributions have a mode of large spot radius at high latitude with higher inclination angle than the mode of the truncated normal prior distribution. Thus, the light curves are also optimized by the 2-spot model with fixed $\sin i$. Table 1 and 2 show the modes of the deduced posterior distributions, their credible regions, and the model evidence for each model, together with the input values and their prior distributions for each of the parameters. Figure 1, 3, 5 and 7, 9, 11 show the results of the 2-spot-like case and 1-spot-like case, respectively: (a) the light curve produced with the input values of the parameters (gray), that reproduced with each mode of the deduced unimodal posterior distribution (red), and their residuals (black) and (b) the temporal radius variation of each spot produced with the input values of the parameters (gray), and those for the 3-spot model, 2-spot model, and 2-spot model with fixed $\sin i$ (red, blue, and green), respectively. The inclination angle, degree of differential rotation, relative intensity, latitude, and radius have degeneracies between any of them. Their joint posterior distributions are delineated in Figure 2, 4, and 6 for the 2-

spot-like case and Figure 8, 10, and 12 for the 1-spot-like case generated using open software `corner` (Foreman-Mackey 2016). The calculated spots on the stellar surface and the light curves are visualized in Figure 13 and 14. We discuss each degeneracy between the parameters in Section 3.1, model selection determining the number of spots in Section 3.2, and the effects on estimating spot lifetime in Section 3.3.

3.1. *Degeneracy between parameters*

Inclination angle vs Spot latitude:

Inclination and each spot latitude are not uniquely deduced under uniform prior distributions due to the degeneracies (Eker 1996; Walkowicz et al. 2013). Therefore, the sine of the inclination angle is constrained as a truncated normal prior distribution with the center equivalent to the input value ($= \sin 60^\circ$) and with the variance ($= 0.15^2$) based on currently achieved precision of spectroscopy (Tables 1 and 2) (Nogami et al. 2014; Notsu et al. 2013a, 2015a,b, 2019). Then, posterior distributions of the inclination angle and spot latitudes are unimodally and adequately deduced from the photometric light curve. We note that the posterior distributions of the inclination angle deduced from the light curve is likely to have a higher accuracy than that would be deduced from real data.

Spot relative intensity vs Spot radius:

Spot relative intensity and each spot size are not uniquely deduced under the uniform prior distributions due to the degeneracies (Walkowicz et al. 2013). Therefore, the spot relative intensity is constrained as a normal prior distribution with the center equivalent to the input value ($= 0.30$) and with the variance ($= 0.05^2$) adopted from a formula of the spot temperature based on the Doppler imaging technique (Tables 1 and 2) (e.g., Berdyugina 2005). Then, the spot relative intensity and each spot radius are unimodally and adequately deduced from the photometric light curve. We note that the posterior distributions of the relative intensity deduced from the light curve is also likely to have a higher accuracy than that would be deduced from real data.

Differential rotation vs Spot latitude: There are degeneracies between the degree of differential rotation and the spot latitudes due to adjusting the periodicity for each spot (Equation 13). However, the deduction of the spot latitude depends on that of the inclination angle, and thus the degree of differential rotation is unimodally deduced from the photometric light curve only if the number of spots is more than two.

Spot latitude vs Spot radius:

There are degeneracies between spot latitudes and the spot radii because the same modulation amplitude is generated by adjusting the parameters (cf. Namekata et al. 2020). However, the deduction of the spot latitude depends on that of the inclination angle, and thus the spot radius is unimodally deduced from the photometric light curve. We note that when the inclination angle becomes too small, the spots are always visible and do not significantly modulate the light curve.

3.2. *Model selection: How many spots exist?*

More spots are observationally indicated to exist than seen in the light curve (Morris et al. 2017; Namekata et al. 2020), whereas the light curve produced with many spots is similar to that with 2 spots or 1 spot (Eker 1994; Basri 2018). Then, we determine the number of spots based on model selection in the Bayesian framework (Kass & Raftery 1995). We compute the model evidence using the importance sampling algorithm along with the parallel tempering

transition and compare each model. The values of the model evidence $\log \mathcal{Z}$ are listed in the Table 1 and 2. In both of cases, the 3-spot model is much more decisive than the 2-spot model and the 2-spot model with fixed $\sin i$ by orders of magnitude: for the 2-spot-like case, the evidence of the 3-spot model relative to that of the 2-spot model and the 2-spot model with fixed $\sin i$ are $\Delta \log \mathcal{Z} = 2639.880$ and 2750.157, respectively. For the 1-spot-like one, they are $\Delta \log \mathcal{Z} = 900.968$ and 951.955, respectively. The difference of the values of the model evidence for the 2-spot-like light curve is much larger than that of the 1-spot-like one because the 2-spot-like one is much more informative to deduce spot properties, such as spot emergence and decay rates (Namekata et al. 2019). In addition, when optimizing light curves by the 4-spot model, the parallel tempering sampling converge to the a multi-modal distribution with much peaks and with degeneracies between the parameters. For the 2-spot-like case, the values of the model evidence of the 4-spot model and the evidence of the 3-spot model relative to that of the 4-spot model are $\log \mathcal{Z} = 60257.257$ and $\Delta \log \mathcal{Z} = 0.314$, respectively. For the 1-spot-like case, they are $\log \mathcal{Z} = 60305.432$ and $\Delta \log \mathcal{Z} = 1.916$, respectively. Then, the 3-spot model is preferable, and the number of spots can be correctly determined in the case of the synthetic light curve. We note that, when conducting starspot modeling of real data, spots are not completely circular, and small spots can be ignored.

3.3. *Effect on estimating spot emergence and decay rates*

The number of spots can directly affect measuring emergence and decay rates. For instance, when optimizing the light curve produced with 3 spots by the 2-spot models, 2 spots out of 3 spots behave as 1. Thus, we qualitatively evaluate an estimation of the spot emergence and decay rates ($\sim \alpha^2_{\mathrm{max},k}/\mathcal{I}_k$, $\alpha^2_{\mathrm{max},k}/\mathcal{E}_k$). Relative to the 3-spot model, the 2-spot model overestimates by a factor of up to 6 because the inclination angle is large and the spot is at high latitude. In the 2-spot model with fixed $\sin i$, the estimates are larger than those of the 3-spot model by a factor of up to 2. These values can have an error of an order of magnitude in the range of the photometic error.

4. CONCLUSION AND FUTURE PROSPECTS

We implement computational code for starspot modeling to deduce stellar and spot properties from photometric brightness modulations. It is implemented with an adaptive parallel tempering algorithm and an importance sampling algorithm for parameter estimation and model selection in the Bayesian framework. In this paper, for evaluating the performance of the code, we apply it to synthetic light curves emulating *Kepler* data of spotted stars. The light curves are specified in the spot parameters, such as the radii, intensities, latitudes, longitudes, and emergence/decay durations, and produced with 3 spots so that they have 2 or 1 local minimum during one equatorial rotation period by adjusting the values of longitude. The spots are circular with specified radii and intensities relative to the photosphere, and the stellar differential rotation coefficient is also included in the light curves. We conduct starspot modeling for the light curves, optimizing by the 3-spot model (Figure 1, 7), 2-spot model (Figure 3, 9), and 2-spot model with fixed $\sin i$ (Figure 5, 11). The calculated spots on the stellar surface and the light curves are visualized (Figure 13, 14). To determine the number of spots, we compare the value of the model evidence for each model. In Section 3, we describe the results, which can be summarized as follows:

(i) Unimodal posterior distributions are deduced in all of the models (Table 1, 2). In the 3-spot model, of course, the modes of the posterior distribution approximately equal the input values of the parameters producing the synthetic light curves. Then, the degeneracies between the parameters are eliminated by constraining the inclination angle and the relative intensity with truncated normal prior distributions (Figure 2, 4, and 6 for 2-spot-like case and Figure 8, 10, and 12 for 1-spot-like case).

(ii) The 3-spot model is decisive because the model evidence is much larger than that of the 2 spot model or 2-spot model with fixed $\sin i$ by orders of magnitude (Table 1, 2). Optimizing light curves by 4-spot model, the parallel tempering sampling converge to a multi-modal distribution with much peaks and with degeneracies between the parameters. Comparing the value of the model evidence with that of the 3-spot model, the 3-spot model is preferable, and the number of spots can be correctly determined in the case of the synthetic light curve.

(iii) Spot emergence and decay rates can be estimated within an error less than an order of magnitude, considering the 3-spot model, 2-spot model, and 2-spot model with fixed $\sin i$.

In the following paper (Paper II), we intend to conduct starspot modeling for *Kepler* and *TESS* data of spotted stars. In particular, *Kepler* data include solar-type stars on which superflares are reported (Notsu et al. 2019, Okamoto et al. 2020 in preparation). We note that *Kepler* data include a long-term trend and instrumental noise, and their unspotted level is unknown (e.g., Basri 2018). It is also necessary to determine the inclination angle precisely by another method, such as spectroscopic observation, when conducting starspot modeling. Then, we can investigate the connection between superflares and stellar and spot properties deduced by starspot modeling and compare the results of measuring emergence and decay rates with those by other methods (Namekata et al. 2020). Bright spotted stars have been observed by *TESS* (Ricker et al. 2014), and superflares on hundreds of spotted solar-type stars have been reported (Tu et al. 2020; Feinstein et al. 2020). Some *TESS* targets are to be simultaneously observed by the *Seimei* telescope in Kyoto University (Kurita et al. 2020) using the high dispersion spectrograph. This could allow us to obtain informative prior knowledge for conducting starspot modeling of *TESS* data.

ACKNOWLEDGMENTS

K.I. sincerely appreciates Makoto Uemura for his statistical advices and Naoto Kojiguchi for his technical advices on *Python* programming. Numerical computations were carried out on the PC cluster at Center for Computational Astrophysics, National Astronomical Observatory of Japan and a Cray XC40 at the Yukawa Institute for Theoretical Physics, Kyoto University. Our study was also supported by JSPS KAKENHI Grant Numbers JP25120007(TK), JP16H03955(KS), JP16J00320(YN), JP16J06887(SN), JP17H02865(DN), JP17K05400(HM), and JP18J20048(KN).

REFERENCES

Almenara, J. M., Díaz, R. F., Dorn, C., et al. 2018, MNRAS, 478, 460
Andrieu, C., & Thoms, J. 2008, Statistics and Computing, 18, 343
Araki, T., & Ikeda, K. 2013, Neural Networks, 43, 33
Arkhypov, O. V., Khodachenko, M. L., Lammer, H., et al. 2018, MNRAS, 473, L84
Basri, G., Walkowicz, L. M., Batalha, N., et al. 2010, ApJL, 713, L155
Basri, G., & Nguyen, H. T. 2018, ApJ, 863, 190
Basri, G. 2018, ApJ, 865, 142
Berdyugina, S. V. 2005, Living Reviews in Solar Physics, 2, 8
Bradshaw, S. J., & Hartigan, P. 2014, ApJ, 795, 79
Brooks, S. P., & Gelman, A. 1992, Journal of Computational and Graphical Statistics, 7, 434
Cox, A. N. 2000, Allen's Astrophysical Quantities
Croll, B., Walker, G. A. H., Kuschnig, R., et al. 2006, ApJ, 648, 607
Croll, B. 2006, PASP, 118, 1351
Davenport, J. 2015, Ph.D. Thesis
Díaz, R. F., Almenara, J. M., Santerne, A., et al. 2014, MNRAS, 441, 983
Eker, Z. 1994, ApJ, 420, 373
Eker, Z. 1996, ApJ, 473, 388

Feinstein, A. D., Montet, B. T., Ansdell, M., et al. 2020, arXiv e-prints, arXiv:2005.07710

Ford, E. B. 2005, AJ, 129, 1706

Ford, E. B. 2006, ApJ, 642, 505

Foreman-Mackey, D., Hogg, D. W., Lang, D., et al. 2013, PASP, 125, 306

Foreman-Mackey, D. 2016, The Journal of Open Source Software, 1, 24

Frasca, A., Fröhlich, H.-E., Bonanno, A., et al. 2011, A&A, 532, A81

Fröhlich, H.-E., Frasca, A., Catanzaro, G., et al. 2012, A&A, 543, A146

Gelman, A., & Rubin, D. B. 1992, Statistical Science, 7, 457

Giles, H. A. C., Collier Cameron, A., & Haywood, R. D. 2017, MNRAS, 472, 1618

Gray, D. F. 2008, The Observation and Analysis of Stellar Photospheres

Gregory, P. C. 2005, Bayesian Logical Data Analysis for the Physical Sciences: A Comparative Approach with 'Mathematica' Support. (Cambridge University Press)

Gregory, P. C. 2005, ApJ, 631, 1198

Haario H., Saksman E., Tamminen J., 2001, Bernoulli, 223

Hastings, W. K. 1970, Biometrika, 57, 97

Henry, G. W., Eaton, J. A., Hamer, J., et al. 1995, ApJS, 97, 513

Hogg, D. W., & Foreman-Mackey, D. 2018, ApJS, 236, 11

Hukushima, K., & Nemoto, K. 1996, Journal of the Physical Society of Japan, 65, 1604

Karoff, C., Knudsen, M. F., De Cat, P., et al. 2016, Nature Communications, 7, 11058

Kass R. E., & Raftery A. E., 1995, J. Am. Stat. Assoc., 90, 773

Kipping, D. M. 2012, MNRAS, 427, 2487

Koch, D. G., Borucki, W. J., Basri, G., et al. 2010, ApJL, 713, L79

Kurita, M., Kino, M., Iwamuro, F., et al. 2020, PASJ, 72, 48

Lanza, A. F., Das Chagas, M. L., & De Medeiros, J. R. 2014, A&A, 564, A50

Maehara, H., Shibayama, T., Notsu, S., et al. 2012, Nature, 485, 478

Maehara, H., Notsu, Y., Notsu, S., et al. 2017, PASJ, 69, 41

Metropolis, N., Rosenbluth, A. W., Rosenbluth, M. N., Teller, A. H., & Teller, E. 1953, JChPh, 21, 1087

Montet, B. T., Tovar, G., & Foreman-Mackey, D. 2017, ApJ, 851, 116

Morris, B. M., Hebb, L., Davenport, J. R. A., et al. 2017, ApJ, 846, 99

Mosser, B., Baudin, F., Lanza, A. F., et al. 2009, A&A, 506, 245

Namekata, K., Maehara, H., Notsu, Y., et al. 2019, ApJ, 871, 187

Namekata, K., Davenport, J. R. A., Morris, B. M., et al. 2020, ApJ, 891, 103

Neal, R. M. 1996, Statistics and Computing, 6, 353

Neal, R. M. 2001, Statistics and Computing, 11, 125

Nelson, B., Ford, E. B., & Payne, M. J. 2014, ApJS, 210, 11

Nogami, D., Notsu, Y., Honda, S., et al. 2014, PASJ, 66, L4

Notsu, S., Honda, S., Notsu, Y., et al. 2013a, PASJ, 65, 112

Notsu, Y., Shibayama, T., Maehara, H., et al. 2013b, ApJ, 771, 127

Notsu, Y., Honda, S., Maehara, H., et al. 2015a, PASJ, 67, 32

Notsu, Y., Honda, S., Maehara, H., et al. 2015b, PASJ, 67, 33

Notsu, Y., Maehara, H., Honda, S., et al. 2019, ApJ, 876, 58

Reinhold, T., Reiners, A., & Basri, G. 2013, A&A, 560, A4

Ricker, G. R., Winn, J. N., Vanderspek, R., et al. 2014, Proc. SPIE, 914320

Robbins, H., & Monro, S. 1951, The Annals of Mathematical Statistics, 22, 3, 400

Roberts, G. O., Gelman, A., Gilks,W. R. 1997, Ann. Appl. Probability, 7, 110

Roberts G. O., Rosenthal J. S., 1998, Can. J. Stat., 26, 5

Savanov, I. S., & Strassmeier, K. G. 2008, Astronomische Nachrichten, 329, 364

Sing, D. K. 2010, A&A, 510, A21

Sharma, S. 2017, ARA&A, 55, 213

Shibata, K., Isobe, H., Hillier, A., et al. 2013, PASJ, 65, 49

Shibayama, T., Maehara, H., Notsu, S., et al. 2013, ApJS, 209, 5

Strassmeier, K. G., & Bopp, B. W. 1992, A&A, 259, 183

Strassmeier, K. G. 2009, A&A Rv, 17, 251

Toriumi, S., & Wang, H. 2019, Living Reviews in Solar Physics, 16, 3

Tu, Z.-L., Yang, M., Zhang, Z. J., et al. 2020, ApJ, 890, 46

Vousden, W. D., Farr, W. M., & Mandel, I. 2016, MNRAS, 455, 1919

Walker, G. A. H., Croll, B., Kuschnig, R., et al. 2007, ApJ, 659, 1611

Walkowicz, L. M., Basri, G., & Valenti, J. A. 2013, ApJS, 205, 17

Yamada, Y., Uemura, M., Itoh, R., et al. 2020, PASJ, 72, 42

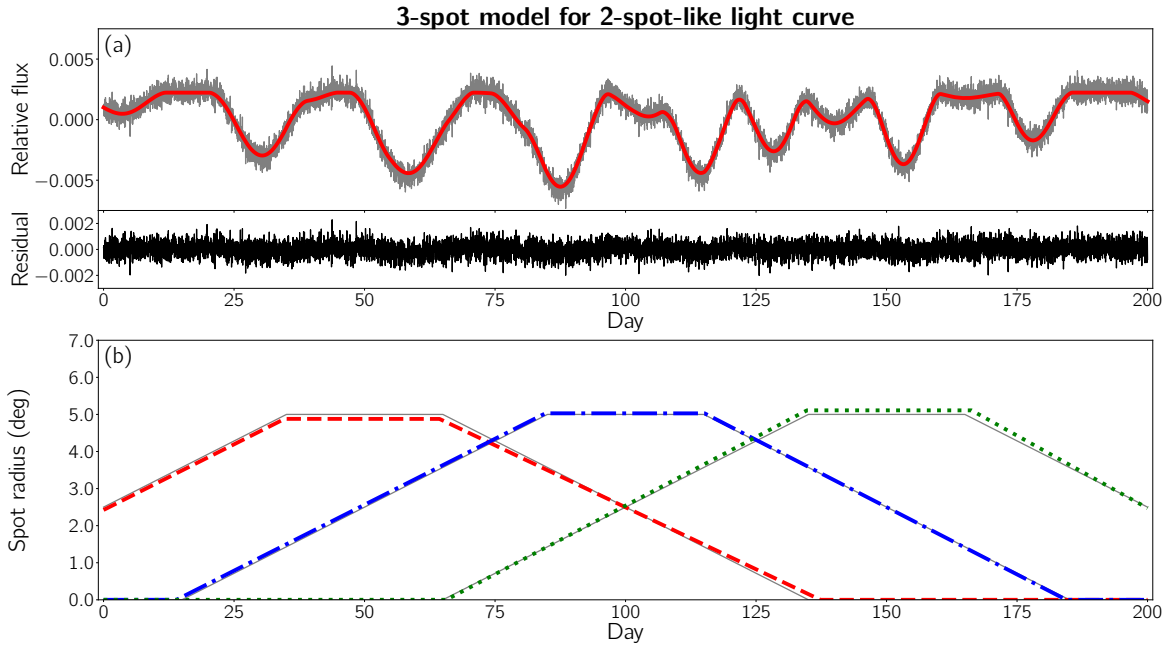

Figure 1. (a) 2-spot-like light curves produced with the input values of the parameters (gray), those reproduced with each mode of the deduced unimodal posterior distribution for the 3-spot model (red), and their residuals (black); (b) Temporal radius variation of each spot produced with the input values of the parameters (gray), and that of the 3-spot model (red, blue, and green).

Table 1. 2-spot-like light curve case

Deduced parameters	Input value	3-spot model	2-spot model	2-spot model with fixed $\sin i$	Prior distribution[a]
(Stellar parameters)					
1. Sine of inclination angle $\sin i$	0.8660	$0.8346^{+0.0382}_{-0.0090}$	$0.9951^{+0.0005}_{-0.0009}$	0.8660 (*fixed*)	$\mathcal{TN}(0.8660, 0.1500^2, 0.0000, 1.0000)$[b]
2. Equatorial period $P_{\rm eq}$ (day)	25.0000	$25.0431^{+0.0376}_{-0.0525}$	$25.2645^{+0.0152}_{-0.1160}$	$25.3125^{+0.0228}_{-0.0202}$	$\mathcal{U}_{\log}(24.0000, 26.0000)$
3. Degree of differential rotation κ	0.1500	$0.1941^{+0.0002}_{-0.0363}$	$0.1097^{+0.0038}_{-0.0010}$	$0.1642^{+0.0021}_{-0.0022}$	$\mathcal{U}(0.0000, 0.2000)$
(Spot parameters)					
4. Relative intensity $f_{\rm spot}$	0.3000	$0.3356^{+0.0239}_{-0.0772}$	$0.3403^{+0.0351}_{-0.0633}$	$0.3658^{+0.0449}_{-0.0601}$	$\mathcal{TN}(0.3000, 0.0500^2, 0.1500, 0.4500)$ [c]
(*1st spot*)					
5. Latitude Φ_1 (deg)	45.00	$38.14^{+5.52}_{-0.18}$	$77.29^{+0.32}_{-0.45}$	$52.31^{+0.26}_{-0.33}$	$\mathcal{U}(-90.00, 90.00)$
6. Initial longitude Λ_1 (deg)	-35.00	$-34.30^{+0.69}_{-0.71}$	$-26.30^{+0.39}_{-0.41}$	$-26.00^{+0.39}_{-0.41}$	$\mathcal{U}(-180.00, 180.00)$
7. Reference time t_1 (day)	50.00	$49.51^{+0.29}_{-0.33}$	$75.81^{+0.16}_{-0.20}$	$75.93^{+0.16}_{-0.20}$	$\mathcal{U}(0.00, t_2)$[d]
8. Maximum radius $\alpha_{\rm max,1}$ (deg)	5.00	$4.88^{+0.31}_{-0.11}$	$12.81^{+0.29}_{-0.44}$	$5.97^{+0.21}_{-0.28}$	$\mathcal{U}(0.01, 15.00)$
9. Emergence duration $\mathcal{I}_1$ (day)	70.000	$68.917^{+0.832}_{-0.985}$	$82.889^{+1.135}_{-1.087}$	$80.745^{+1.352}_{-0.795}$	$\mathcal{U}_{\log}(0.000, 200.000)$
10. Decay duration $\mathcal{E}_1$ (day)	70.000	$72.996^{+2.941}_{-1.845}$	$75.709^{+0.792}_{-0.985}$	$73.288^{+0.959}_{-0.693}$	$\mathcal{U}_{\log}(0.000, 200.000)$
11. Stable duration $\mathcal{L}_1$ (day)	30.000	$29.645^{+0.530}_{-0.798}$	$62.621^{+0.389}_{-0.462}$	$62.315^{+0.337}_{-0.509}$	$\mathcal{U}_{\log}(0.000, 200.000)$
(*2nd spot*)					
12. Latitude Φ_2 (deg)	30.00	$25.26^{+3.60}_{-0.46}$	$7.57^{+5.43}_{-2.69}$	$-0.29^{+0.62}_{-0.79}$	$\mathcal{U}(-90.00, 90.00)$
13. Initial longitude Λ_2 (deg)	-150.00	$-151.20^{+1.49}_{-1.71}$	$-23.30^{+1.69}_{-1.51}$	$-22.40^{+2.19}_{-1.41}$	$\mathcal{U}(-180.00, 180.00)$
14. Reference time t_2 (day)	100.00	$99.89^{+0.29}_{-0.24}$	$151.95^{+0.43}_{-0.46}$	$152.90^{+0.39}_{-0.47}$	$\mathcal{U}(t_1, t_3)$[d,e]
15. Maximum radius $\alpha_{\rm max,2}$ (deg)	5.00	$4.98^{+0.16}_{-0.21}$	$5.06^{+0.11}_{-0.20}$	$5.67^{+0.21}_{-0.27}$	$\mathcal{U}(0.01, 15.00)$
16. Emergence duration $\mathcal{I}_2$ (day)	70.000	$70.704^{+1.450}_{-1.497}$	$64.258^{+1.167}_{-0.944}$	$70.520^{+0.873}_{-1.182}$	$\mathcal{U}_{\log}(0.000, 200.000)$
17. Decay duration $\mathcal{E}_2$ (day)	70.000	$69.311^{+0.773}_{-0.854}$	$49.009^{+5.633}_{-3.272}$	$41.850^{+5.284}_{-3.237}$	$\mathcal{U}_{\log}(0.000, 200.000)$
18. Stable duration $\mathcal{L}_2$ (day)	30.000	$30.472^{+0.420}_{-0.622}$	$34.450^{+0.928}_{-0.938}$	$35.759^{+0.635}_{-1.175}$	$\mathcal{U}_{\log}(0.000, 200.000)$
(*3rd spot*)					
19. Latitude Φ_3 (deg)	15.00	$12.27^{+2.60}_{-0.59}$	-	-	$\mathcal{U}(-90.00, 90.00)$
20. Initial longitude Λ_3 (deg)	-25.00	$-23.50^{+1.39}_{-1.81}$	-	-	$\mathcal{U}(-180.00, 180.00)$
21. Reference time t_3 (day)	150.00	$150.51^{+0.39}_{-0.48}$	-	-	$\mathcal{U}(t_2, 200.00)$[d]
22. Maximum radius $\alpha_{\rm max,3}$ (deg)	5.00	$5.11^{+0.20}_{-0.19}$	-	-	$\mathcal{U}(0.01, 15.00)$
23. Emergence duration $\mathcal{I}_3$ (day)	70.000	$69.082^{+1.009}_{-1.028}$	-	-	$\mathcal{U}_{\log}(0.00, 200.000)$
24. Decay duration $\mathcal{E}_3$ (day)	70.000	$65.320^{+4.032}_{-4.379}$	-	-	$\mathcal{U}_{\log}(0.00, 200.000)$
25. Stable duration $\mathcal{L}_3$ (day)	30.000	$31.551^{+0.445}_{-1.434}$	-	-	$\mathcal{U}_{\log}(0.00, 200.000)$
Model evidence $\log \mathcal{Z}$		60257.571	57617.691	57507.414	

[a] Each representation of the prior distributions defined in $a \leq \theta \leq b$ are as follows: bounded uniform distribution $\mathcal{U}(a, b) = 1/(b-a)$; log uniform distribution $\mathcal{U}_{\log}(a, b) = \log\theta/\log(b/a)$ known as Jeffey's prior; truncated normal distribution $\mathcal{TN}(\mu, \sigma^2, a, b)$, which equals $\mathcal{N}(\mu, \sigma^2)$ normalized by its cumulative distribution.

[b] The variance value is based on currently achieved precision of spectroscopy (Notsu et al. 2019).

[c] The variance value is adopted from a formula of the spot temperature based on the Doppler imaging technique in the case of solar effective temperature (Berdyugina 2005; Maehara et al. 2017).

[d] We discern each of spot by the reference time t_k: if spots are not discerned, they are replaced one by one during the parallel tempering parameter transition. The number of maxima of the likelihood equals factorial of the number of spots, and the parallel tempering sampling becomes much inefficient.

[e] For the 2-spot model and 2-spot model with fixed $\sin i$, we set $t_3 = 200.000$ (upper limit of the interval of the light curve).

Table 2. 1-spot-like light curve case

Deduced parameters	Input value	3-spot model	2-spot model	2-spot model with fixed $\sin i$	Prior distribution[a]
(Stellar parameters)					
1. Sine of inclination angle $\sin i$	0.8660	$0.8976^{+0.0054}_{-0.0647}$	$0.9874^{+0.0013}_{-0.0024}$	0.8660 (*fixed*)	$\mathcal{TN}(0.8660, 0.1500^2, 0.0000, 1.0000)$ [b]
2. Equatorial period $P_{\rm eq}$ (day)	25.0000	$24.9756^{+0.0550}_{-0.0748}$	$24.4909^{+0.1400}_{-0.1002}$	$25.0607^{+0.0251}_{-0.0526}$	$\mathcal{U}_{\log}(24.0000, 26.0000)$
3. Degree of differential rotation κ	0.1500	$0.1340^{+0.0426}_{-0.0075}$	$0.0467^{+0.0041}_{-0.0057}$	$0.0331^{+0.0028}_{-0.0020}$	$\mathcal{U}(0.0000, 0.2000)$
(Spot parameters)					
4. Relative intensity $f_{\rm spot}$	0.3000	$0.3050^{+0.0487}_{-0.0336}$	$0.2974^{+0.0767}_{-0.0152}$	$0.3518^{+0.0486}_{-0.0609}$	$\mathcal{TN}(0.3000, 0.0500^2, 0.1500, 0.4500)$ [c]
(*1st spot*)					
5. Latitude Φ_1 (deg)	45.00	$48.28^{+2.20}_{-7.76}$	$75.92^{+0.35}_{-0.72}$	$55.38^{+0.22}_{-0.28}$	$\mathcal{U}(-90.00, 90.00)$
6. Initial longitude Λ_1 (deg)	55.00	$54.90^{+0.69}_{-0.81}$	$32.40^{+0.39}_{-0.51}$	$32.60^{+0.49}_{-0.41}$	$\mathcal{U}(-180.00, 180.00)$
7. Reference time t_1 (day)	50.00	$50.21^{+0.42}_{-0.52}$	$83.86^{+0.13}_{-0.23}$	$83.95^{+0.19}_{-0.18}$	$\mathcal{U}(0.00, t_2)$ [d]
8. Maximum radius $\alpha_{\rm max,1}$ (deg)	5.00	$5.06^{+0.40}_{-0.17}$	$11.34^{+0.30}_{-0.54}$	$6.09^{+0.32}_{-0.20}$	$\mathcal{U}(0.01, 15.00)$
9. Emergence duration $\mathcal{I}_1$ (day)	70.000	$67.235^{+2.591}_{-3.003}$	$104.731^{+1.222}_{-1.042}$	$101.301^{+1.131}_{-0.847}$	$\mathcal{U}_{\log}(0.000, 200.000)$
10. Decay duration $\mathcal{E}_1$ (day)	70.000	$69.930^{+4.191}_{-4.629}$	$72.010^{+0.956}_{-1.975}$	$67.904^{+1.130}_{-1.484}$	$\mathcal{U}_{\log}(0.000, 200.000)$
11. Stable duration $\mathcal{L}_1$ (day)	30.000	$30.624^{+0.754}_{-0.940}$	$61.412^{+0.400}_{-0.392}$	$62.004^{+0.354}_{-0.426}$	$\mathcal{U}_{\log}(0.000, 200.000)$
(*2nd spot*)					
12. Latitude Φ_2 (deg)	30.00	$34.08^{+1.61}_{-6.15}$	$45.43^{+2.24}_{-2.82}$	$17.13^{+0.99}_{-1.00}$	$\mathcal{U}(-90.00, 90.00)$
13. Initial longitude Λ_2 (deg)	75.00	$77.90^{+2.59}_{-2.21}$	$-65.60^{+3.29}_{-2.51}$	$-61.30^{+2.59}_{-3.51}$	$\mathcal{U}(-180.00, 180.00)$
14. Reference time t_2 (day)	100.00	$100.68^{+0.46}_{-0.56}$	$150.44^{+1.28}_{-0.93}$	$150.95^{+0.93}_{-1.40}$	$\mathcal{U}(t_1, t_3)$ [d,e]
15. Maximum radius $\alpha_{\rm max,2}$ (deg)	5.00	$5.05^{+0.17}_{-0.14}$	$5.57^{+0.30}_{-0.14}$	$4.99^{+0.21}_{-0.22}$	$\mathcal{U}(0.01, 15.00)$
16. Emergence duration $\mathcal{I}_2$ (day)	70.000	$66.746^{+3.542}_{-2.173}$	$39.158^{+0.775}_{-0.940}$	$38.637^{+0.867}_{-0.852}$	$\mathcal{U}_{\log}(0.000, 200.000)$
17. Decay duration $\mathcal{E}_2$ (day)	70.000	$69.651^{+1.272}_{-1.767}$	$100.786^{+6.404}_{-17.922}$	$97.018^{+8.629}_{-16.458}$	$\mathcal{U}_{\log}(0.000, 200.000)$
18. Stable duration $\mathcal{L}_2$ (day)	30.000	$30.963^{+0.755}_{-0.764}$	$25.394^{+1.430}_{-3.138}$	$24.693^{+1.856}_{-3.006}$	$\mathcal{U}_{\log}(0.000, 200.000)$
(*3rd spot*)					
19. Latitude Φ_3 (deg)	15.00	$15.98^{+1.64}_{-3.22}$	-	-	$\mathcal{U}(-90.00, 90.00)$
20. Initial longitude Λ_3 (deg)	-50.00	$-54.00^{+4.49}_{-2.21}$	-	-	$\mathcal{U}(-180.00, 180.00)$
21. Reference time t_3 (day)	150.00	$149.90^{+0.86}_{-1.37}$	-	-	$\mathcal{U}(t_2, 200.00)$ [d]
22. Maximum radius $\alpha_{\rm max,3}$ (deg)	5.00	$5.04^{+0.15}_{-0.18}$	-	-	$\mathcal{U}(0.01, 15.00)$
23. Emergence duration $\mathcal{I}_3$ (day)	70.000	$70.000^{+3.545}_{-5.136}$	-	-	$\mathcal{U}_{\log}(0.00, 200.000)$
24. Decay duration $\mathcal{E}_3$ (day)	70.000	$71.902^{+15.202}_{-6.103}$	-	-	$\mathcal{U}_{\log}(0.00, 200.000)$
25. Stable duration $\mathcal{L}_3$ (day)	30.000	$29.131^{+1.662}_{-3.178}$	-	-	$\mathcal{U}_{\log}(0.00, 200.000)$
Model evidence $\log \mathcal{Z}$		60307.348	59406.380	59355.393	

[a] Each representation of the prior distributions defined in $a \leq \theta \leq b$ are as follows: bounded uniform distribution $\mathcal{U}(a, b) = 1/(b-a)$; log uniform distribution $\mathcal{U}_{\log}(a, b) = \log\theta/\log(b/a)$ known as Jeffey's prior; truncated normal distribution $\mathcal{TN}(\mu, \sigma^2, a, b)$, which equals $\mathcal{N}(\mu, \sigma^2)$ normalized by its cumulative distribution.

[b] The variance value is based on currently achieved precision of spectroscopy (Notsu et al. 2019).

[c] The variance value is adopted from a formula of the spot temperature based on the Doppler imaging technique in the case of solar effective temperature (Berdyugina 2005; Maehara et al. 2017).

[d] We discern each of spot by the reference time t_k: if spots are not discerned, they are replaced one by one during the parallel tempering parameter transition. The number of maxima of the likelihood equals factorial of the number of spots, and the parallel tempering sampling becomes much inefficient.

[e] For the 2-spot model and 2-spot model with fixed $\sin i$, we set $t_3 = 200.000$ (upper limit of the interval of the light curve).

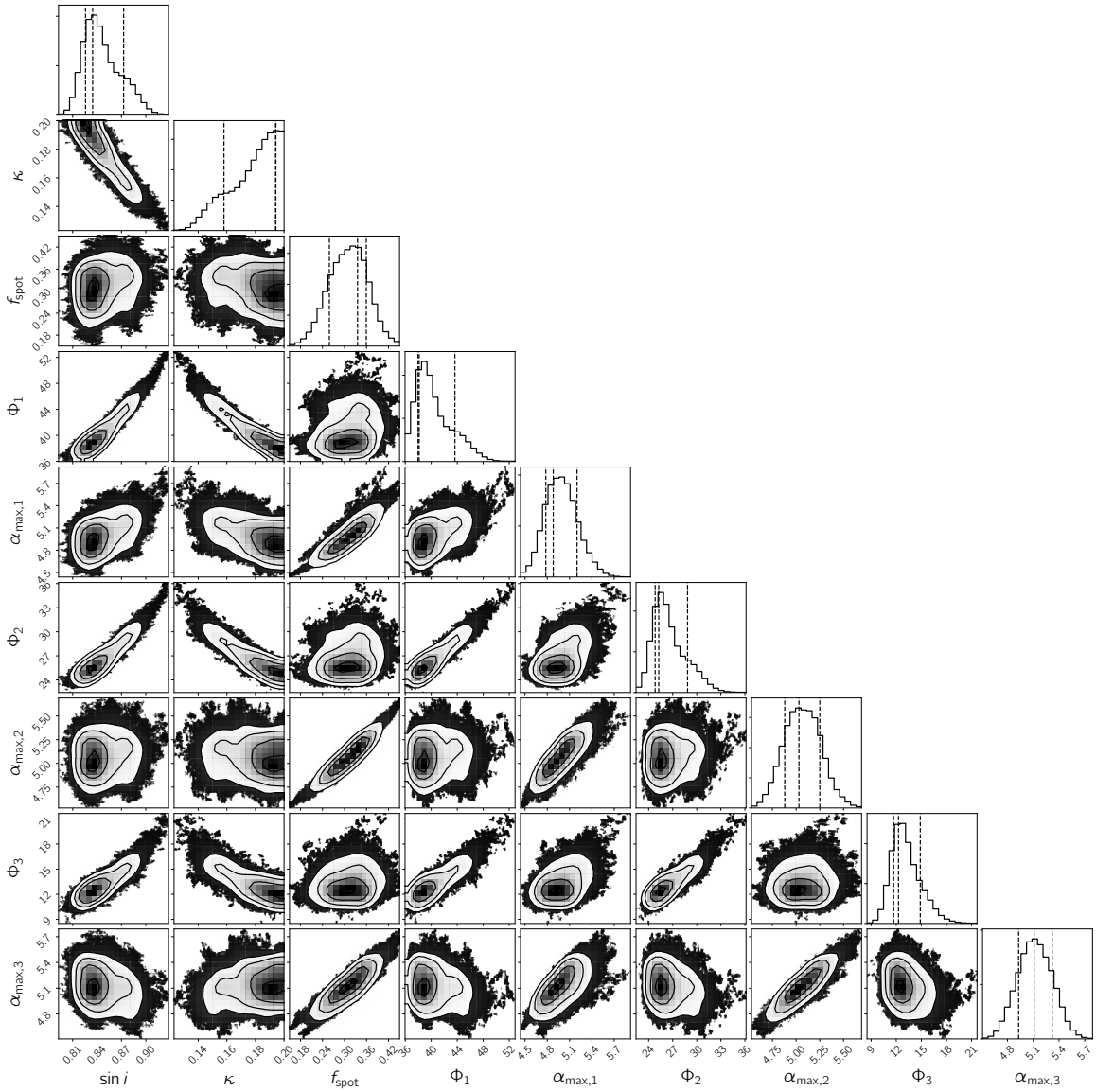

Figure 2. The joint posterior distribution of parameters with the degeneracies for 2-spots-like light curve by the 3-spot model. Each column represents the inclination angle $\sin i$, degree of differential rotation κ, relative intensity $f_{\rm spot}$, maximum radius $\alpha_{{\rm max},k}$, and latitude Φ_k.

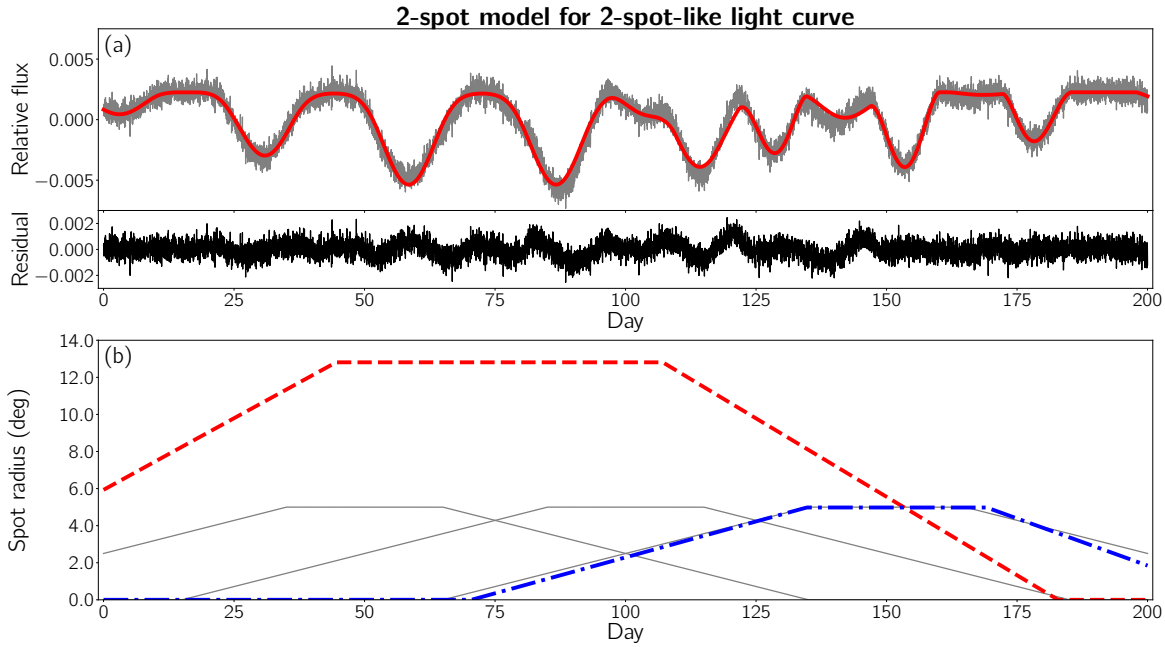

Figure 3. (a,b) The same as Figure 1 but for the 2-spot model.

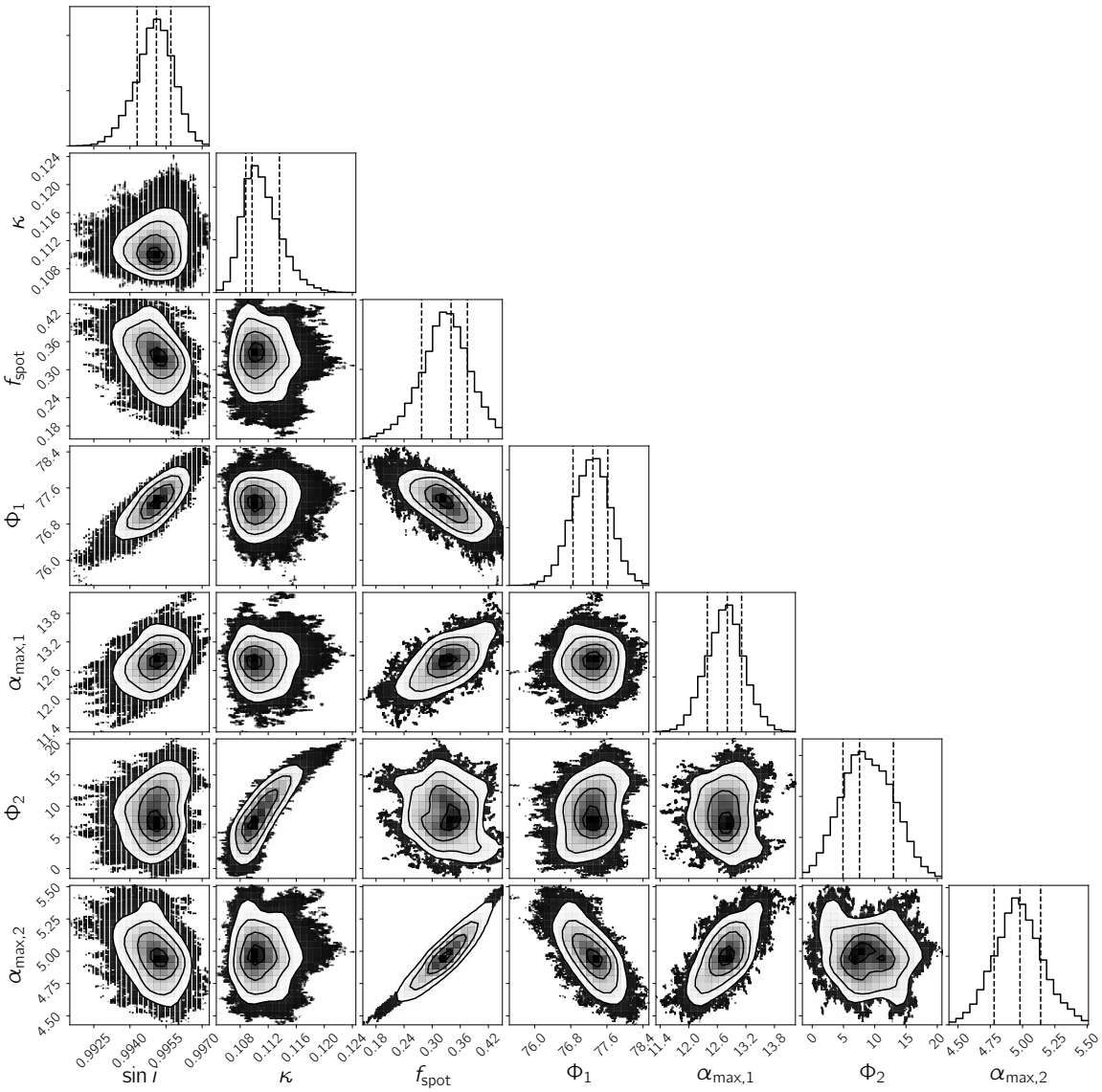

Figure 4. The same as Figure 2 but for the 2-spot model.

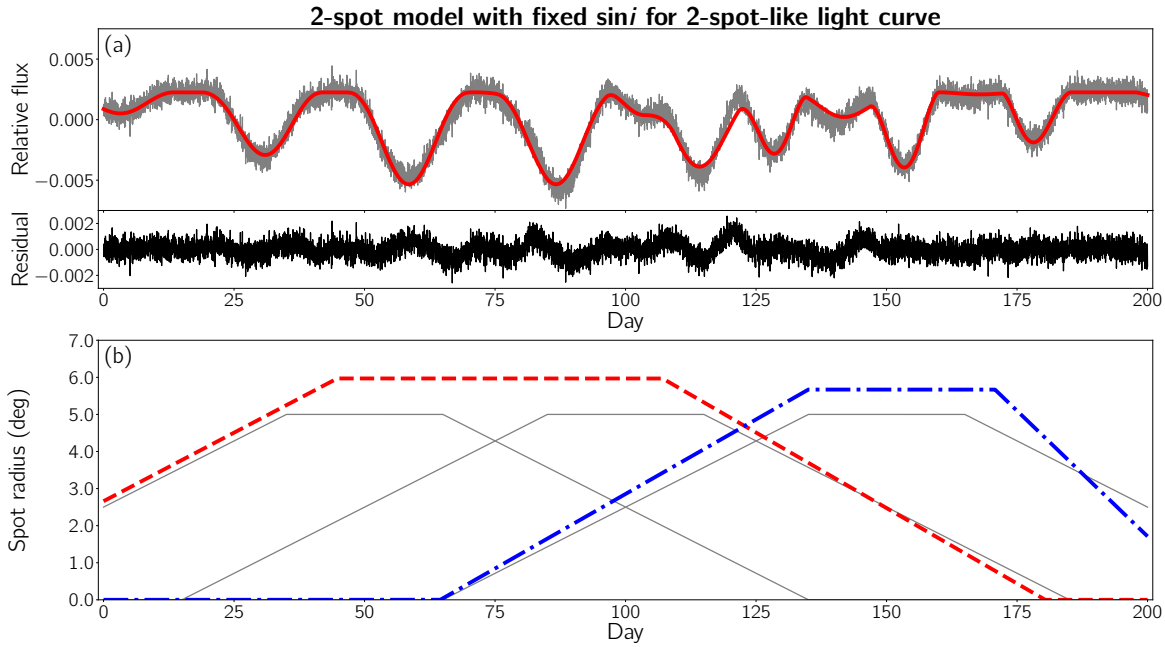

Figure 5. (a,b) The same as Figure 1 but for the 2-spot model with fixed $\sin i$.

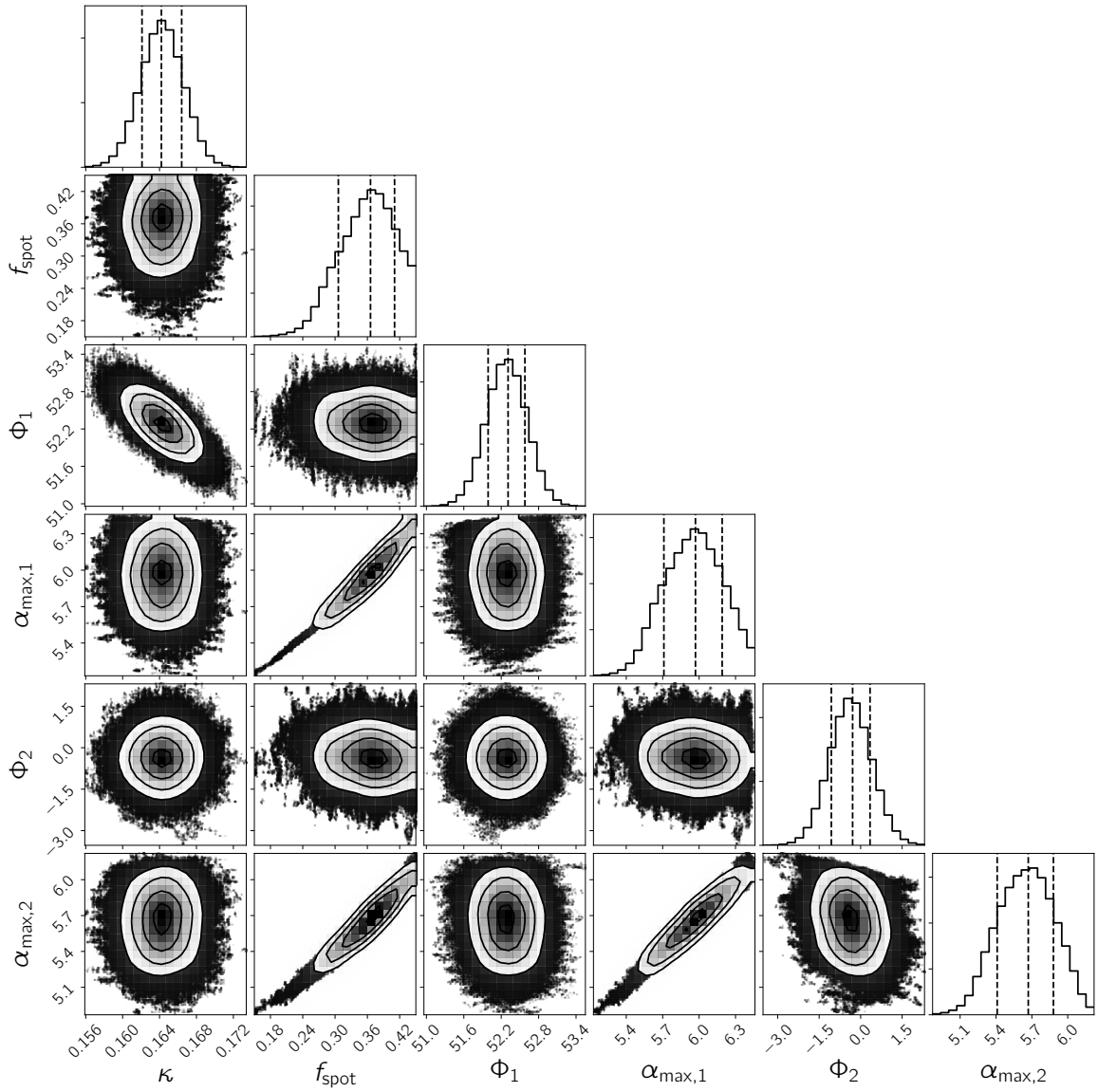

Figure 6. The same as Figure 2 but for the 2-spot model with fixed $\sin i$.

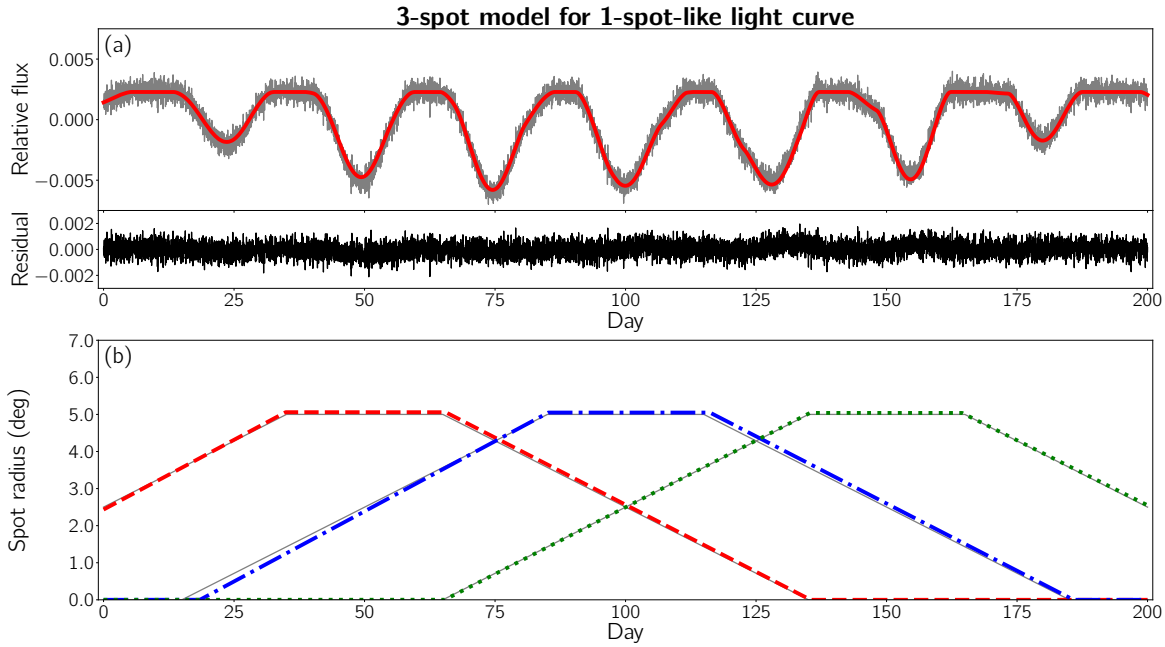

Figure 7. (a) 1-spot-like light curves produced with the input values of the parameters (gray), those reproduced with each mode of the deduced unimodal posterior distribution for the 3-spot model (red), and their residuals (black); (b) Temporal radius variation of each spot produced with the input values of the parameters (gray), and that of the 3-spot model (red, blue, and green).

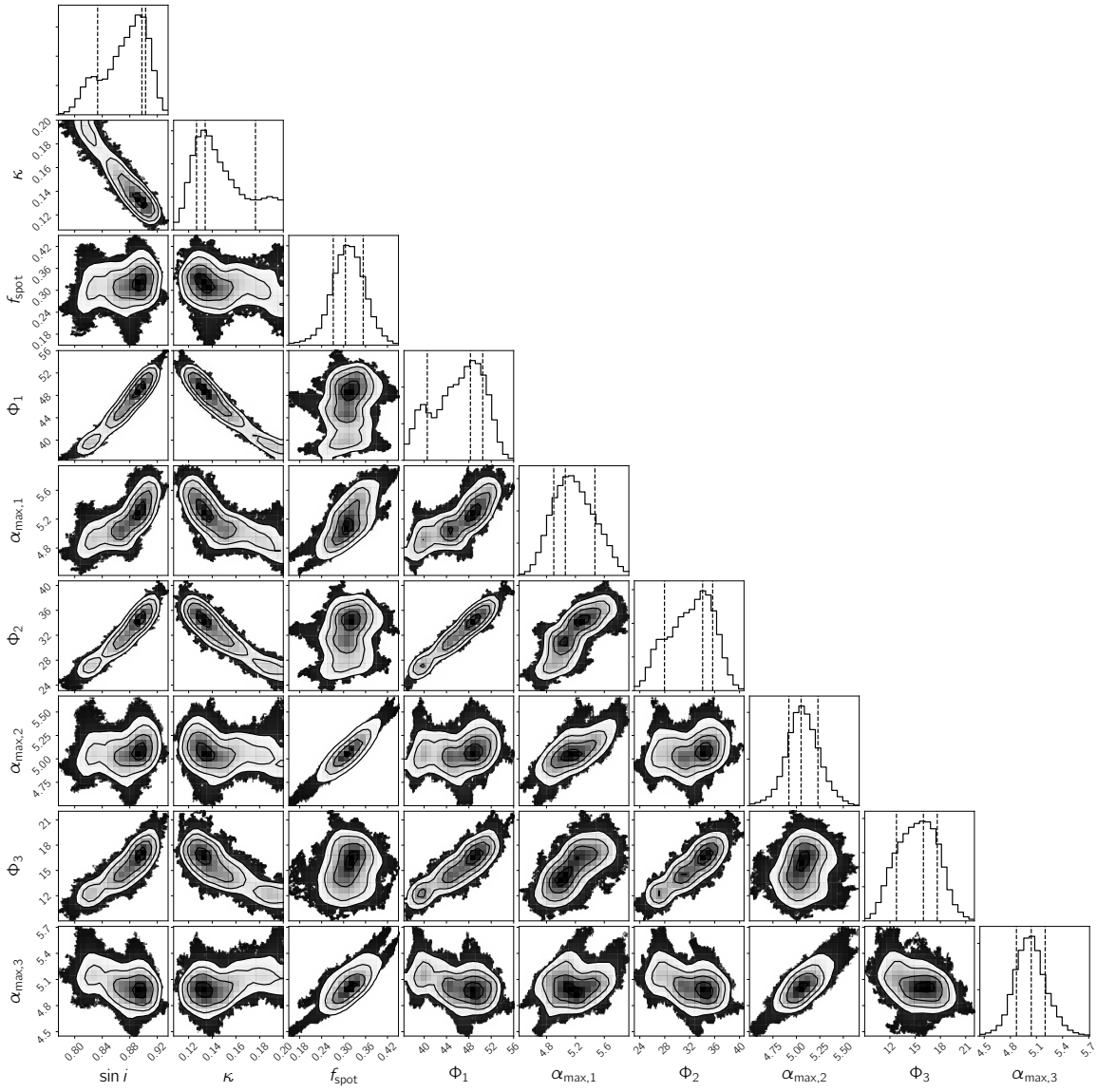

Figure 8. The joint posterior distribution of parameters with the degeneracies for 1-spots-like light curve by the 3-spot model. Each column represents the inclination angle $\sin i$, degree of differential rotation κ, relative intensity $f_{\rm spot}$, the maximum radius $\alpha_{\rm max,k}$, and latitude Φ_k.

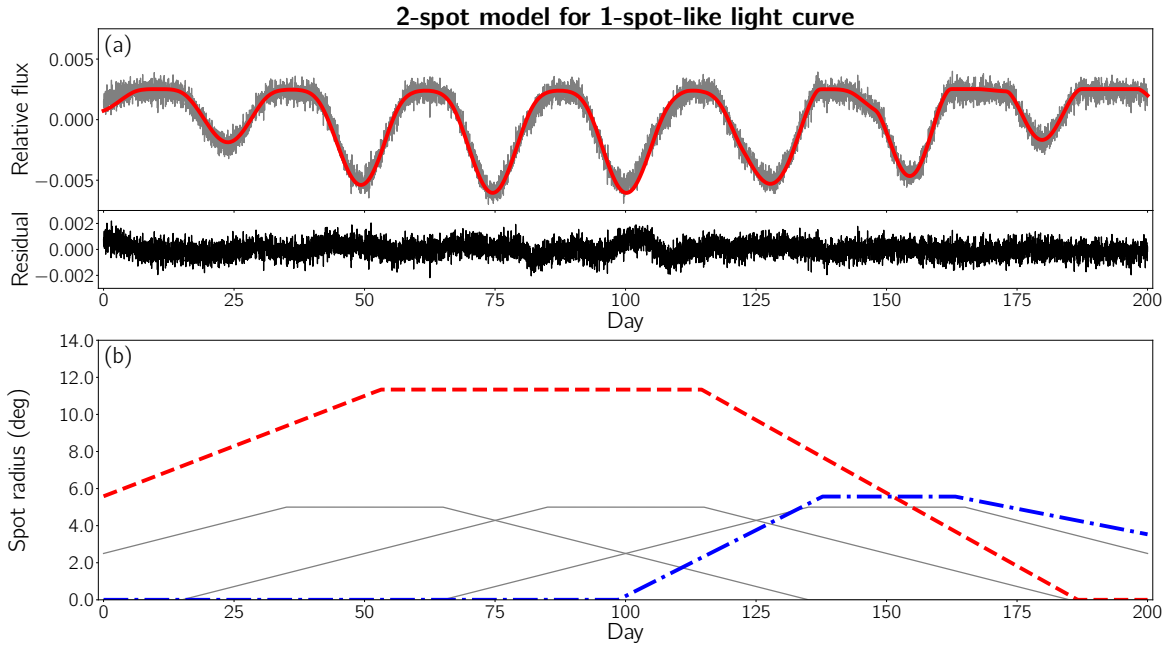

Figure 9. (a,b) The same as Figure 7 but for the 2-spot model.

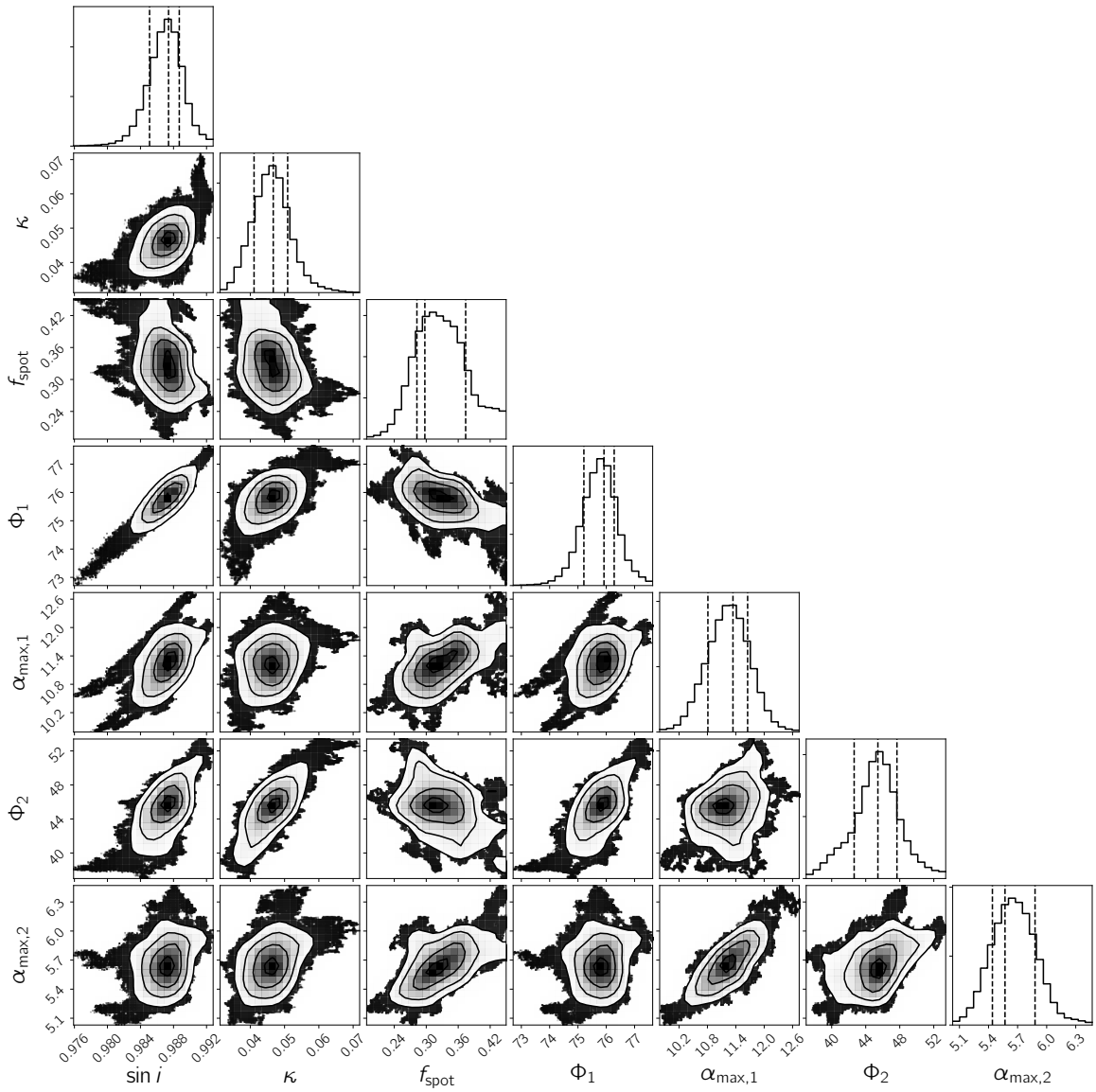

Figure 10. The same as Figure 8 but for the 2-spot model.

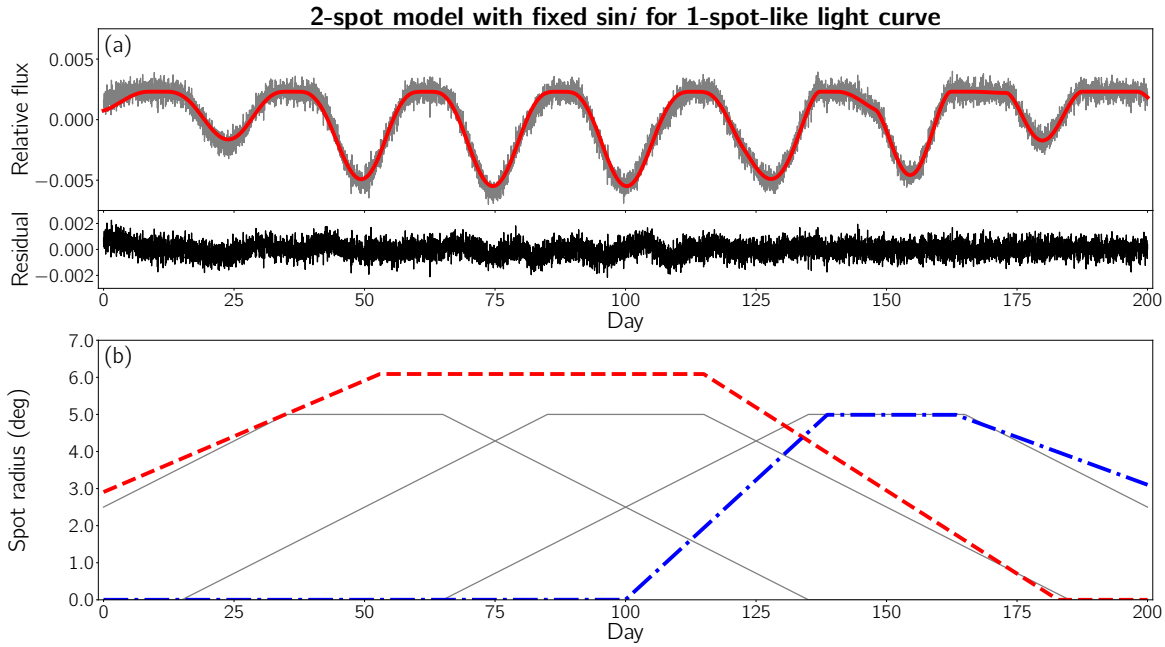

Figure 11. (a,b) The same as Figure 7 but for the 2-spot model with fixed $\sin i$.

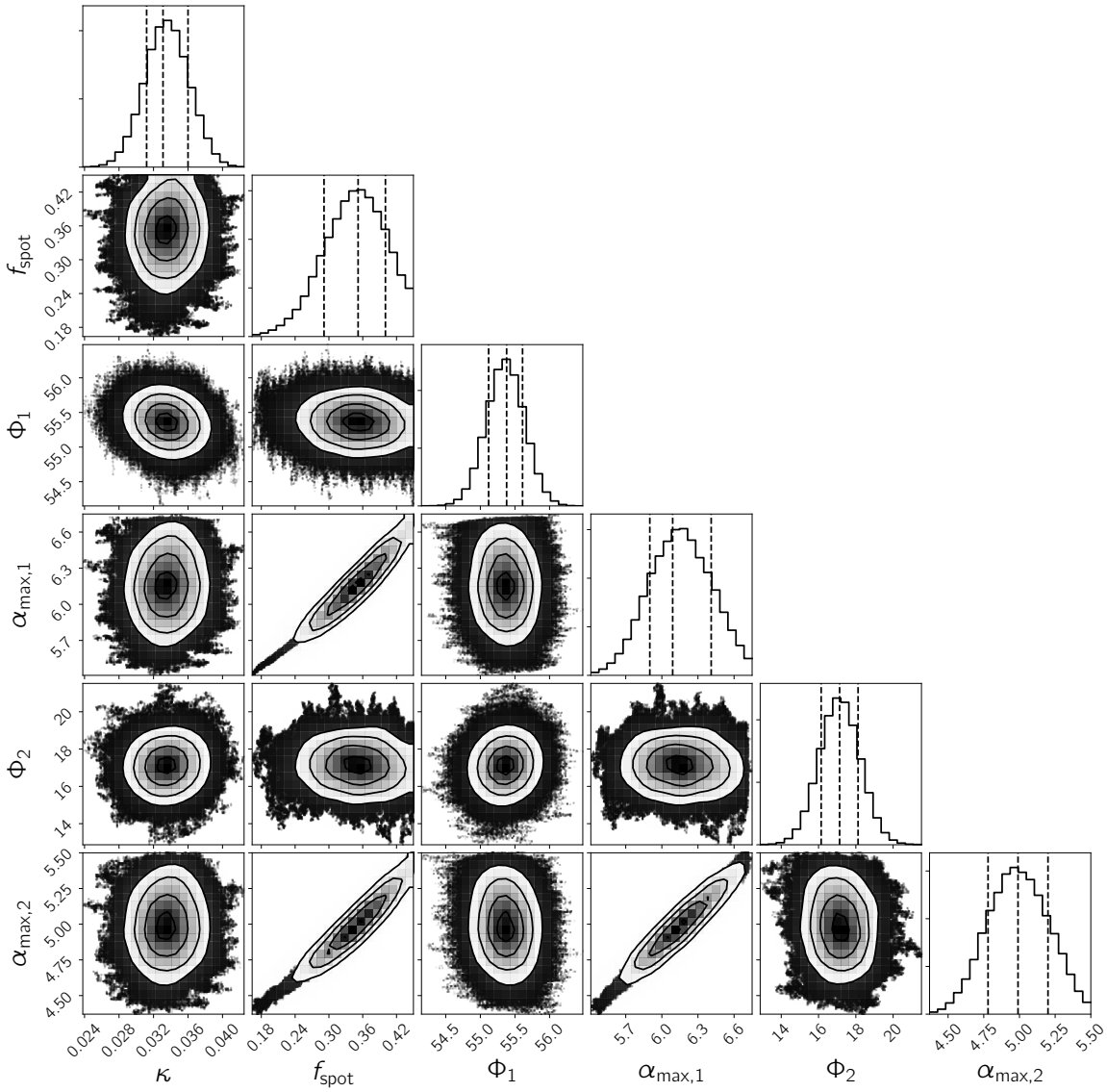

Figure 12. The same as Figure 8 but for the 2-spot model with fixed $\sin i$.

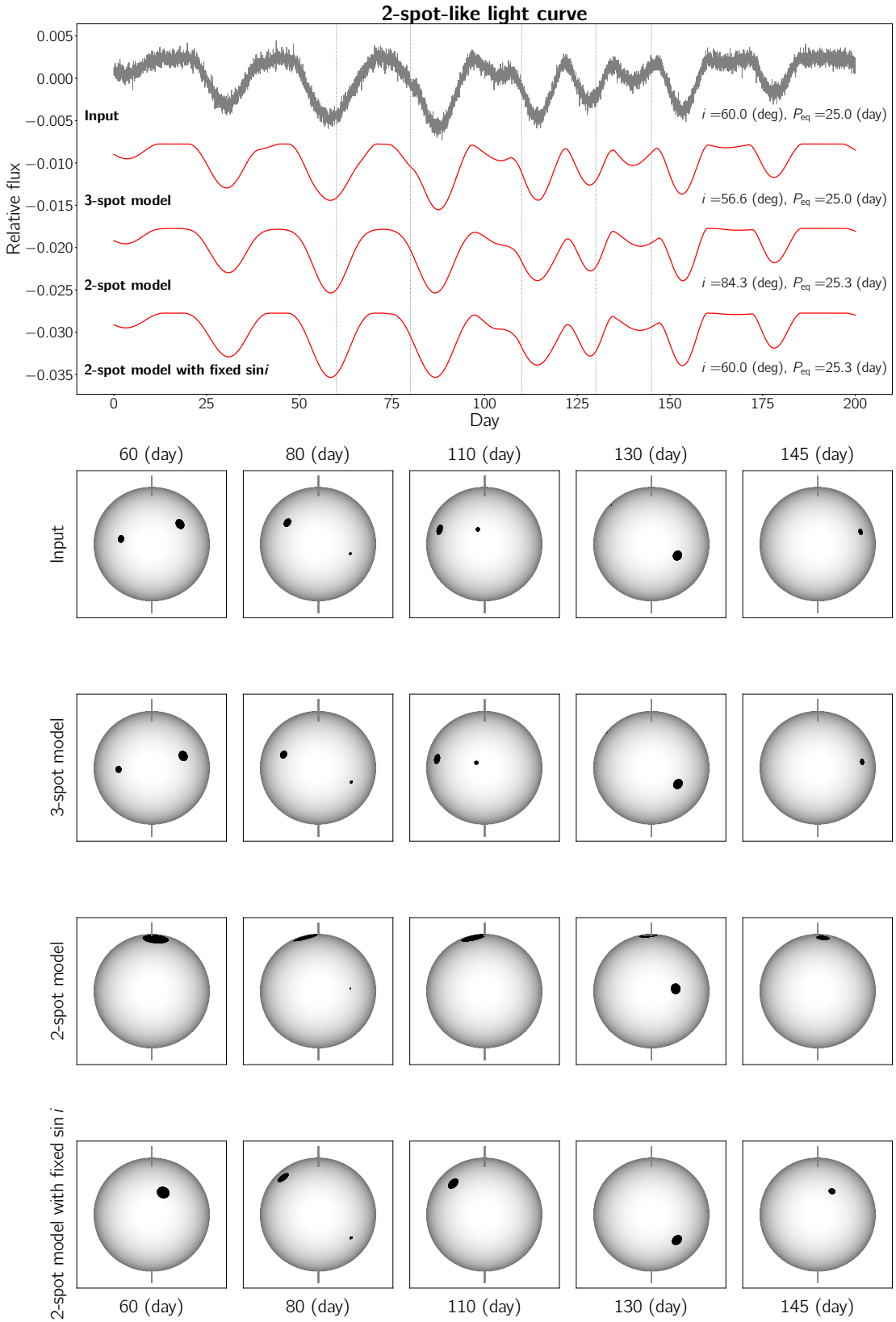

Figure 13. The input light curve (gray) and the ones reproduced by the optimum of each of the models (red) for the 2-spot-like case. The values of the inclination angle and the equatorial period are also denoted for each of the models. The calculated spots on the stellar surface are visualized at five times (vertical dotted lines).

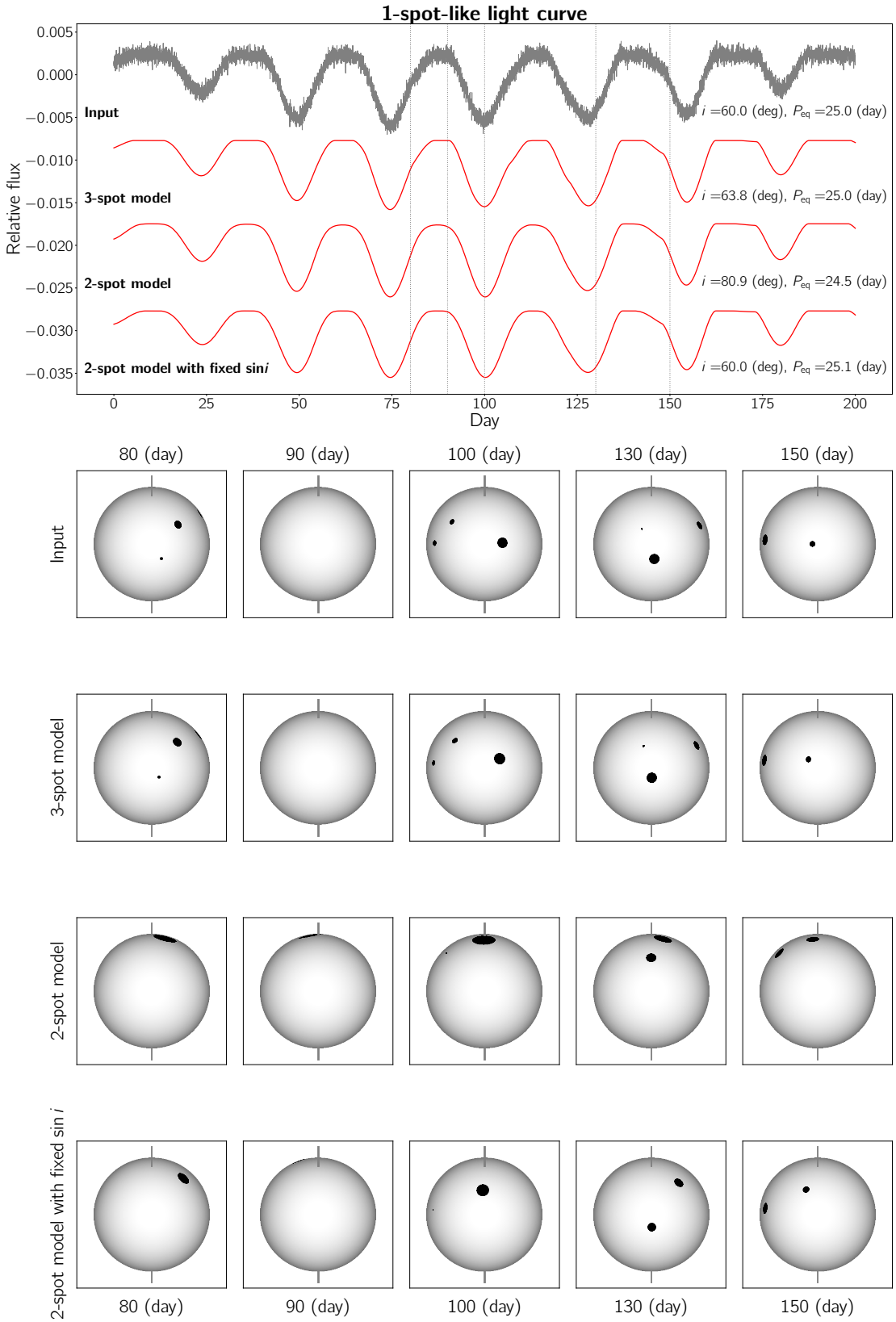

Figure 14. The same as Figure 13 but for the 1-spot-like case.